Magnetic Ground State of a Thin-Film Element

Wolfgang Rave, *Member, IEEE,* and Alex Hubert, *Senior Member, IEEE*

Abstract—By means of three-dimensional numerical calculations we studied possible micromagnetic configurations in a rectangular Permalloy-like thin-film element. The parameters were chosen to be compatible with the so-called micromagnetic standard problem 1. We demonstrate that for these parameters a diamond domain pattern is the lowest energy state that replaces cross-tie patterns favorable in larger elements. Only at smaller sizes does the originally envisaged Landau pattern form the ground state. The transition to high-remanence structures (or what would be comparable to a "single-domain" state) is found for lateral sizes that are an order of magnitude smaller than the benchmark parameters. The transitions among the different domain patterns become plausible in view of the energy of symmetric Néel walls in extended thin films. The features of the high-remanence structures can be derived from the principle of uniform charge distribution.

Index Terms—Benchmark, numerical micromagnetics, standard problems, thin-film elements.

I. INTRODUCTION

WHILE in the days of W. F. Brown *micromagnetics* [1] was an art for mathematically inclined physicists, it has nowadays turned to a relatively widespread "engineering" activity. This development was caused by the availability of inexpensive, powerful computers and led to a considerable increase in the number of publications in numerical micromagnetism. Nevertheless, the micromagnetic equations (at least until today) have not become a problem of pure number crunching, which might be attributed to their main difficulty, which lies in solving the nonlocal magnetostatic equations in every step of the energy minimization.

This situation led to a number of doubtful results and to the need for reliable reference solutions of typical micromagnetic problems. To satisfy this demand, a few years ago, a micromagnetics modeling activity group at the National Institute of Standards and Technology (NIST) was founded and the so-called standard problem 1 (SP1) was established [2]. This problem asked for the hysteresis loop of a 2-μm $\times$ 1-μm $\times$ 0.02-μm thin-film element with material parameters that were not too different from what could be called Permalloy (the exact reduced anisotropy constant in SP1 is $Q = K_u/K_d = 0.0024$, markedly larger than that of true Permalloy, which is usually described by $Q = 0.00025$). As abbreviations for the material constants, we use K_u = uniaxial anisotropy constant, $K_d = \mu_0 M_s^2/2$ = stray field energy constant, and A = exchange constant. The values of the benchmark problem that are used throughout this paper are $K_u = 500$ J/m^3, $M_s = 8 \times 10^5$ A/m, and $A = 1.3 \times 10^{-11}$ J/m).

The anonymously submitted results to this benchmark problem were rather disappointing [2], however, because calculated coercivity values or switching fields differed by as much as a factor of 100, provoking comments on the general unreliability of numerical micromagnetic computations [3], [4].

Beside the trivial explanation with programming errors[1] or serious underdiscretization (which seems undeniable for at least some of the submitted solutions when we look at the presented vector and grayscale plots; see [2]), a less trivial reason for the large discrepancies observed could have been that the magnetic starting patterns were different for these simulations. We considered the knowledge about the magnetic ground state and the most important metastable states already in itself useful for a better understanding of a magnetic thin-film element [5].

Our answer to this question for the particular case of the parameters of SP1 will be described in Section II. To this end, the total energy of eight configurations in zero field was calculated with finite element methods extrapolated to infinitely fine discretization. In this way, the total micromagnetic energy of the investigated metastable states could be reliably determined and the lowest energy configuration could be identified.

Section III extends these calculations to elements of different lateral size (keeping the film thickness constant). We demonstrate that, depending on size, five different configurations represent the lowest energy state. A calculation of the energy of symmetric Néel walls in extended films for different wall angles serves to understand the reason why the Landau pattern gets replaced by other domain patterns in large elements. Finally, Section IV is an attempt to achieve a better understanding of the various configurations by constructing domain models in such a way that their energy comes close to the equilibrium energies. Such domain models could be extended to parameter combinations that are still outside of the range of micromagnetic calculations.

II. GROUND STATE AND METASTABLE STATES FOR STANDARD PROBLEM 1

Already in a thin-film element of moderate size, we find a surprising variety of possible magnetic states that can exist as metastable solutions and that were partially investigated in several papers, e.g., [6]–[11]. Bearing these in mind, but also guided

[1]Of course, we also cannot exclude errors for the present calculations. However, we checked some results against independent calculations of other colleagues. The observation of a discrepancy between our results and those of [11] led to the discovery of a problem of the vector potential method in dealing with situations in which the demagnetizing field is very small. Calculations by R. Hertel, using the scalar potential, yielded again agreement with our results. Another comparison for one specific set of parameters with an independent calculation by J. Miltat, Orsay, also gave satisfactory agreement with our results.
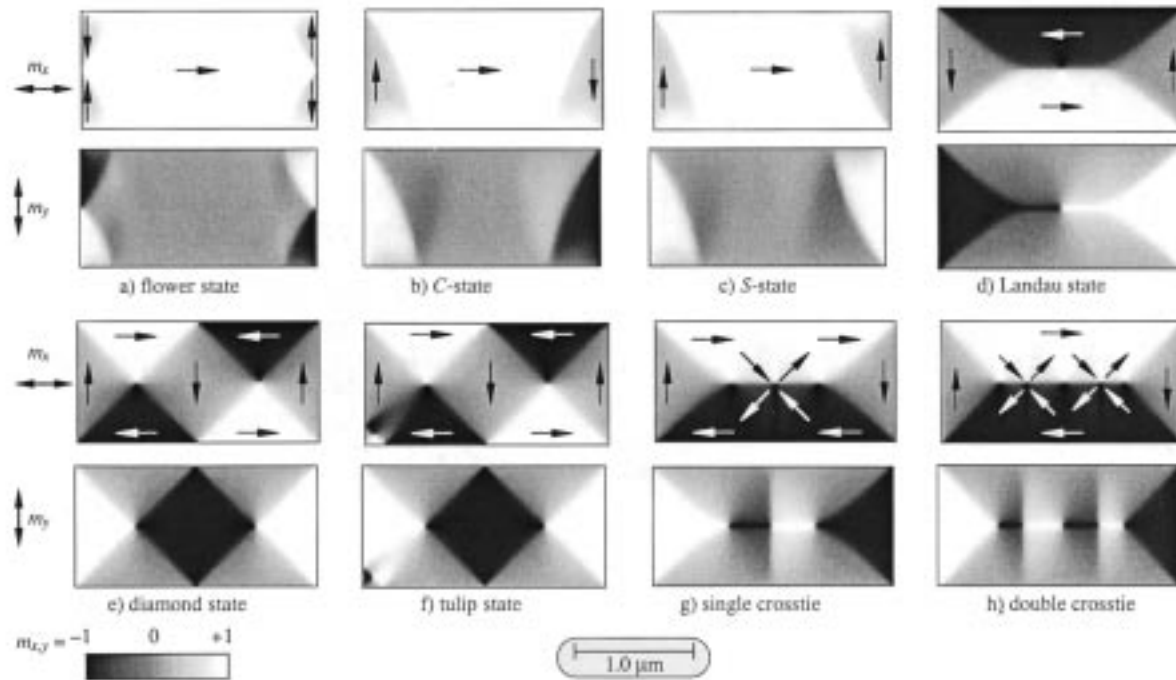
Fig. 1.   Investigated magnetization patterns for a rectangular thin-film element. Numerically calculated equilibrium structures for the parameters of SP1 are presented by pairs of grayscale plots. For each configuration in the upper image contrast due to the magnetization, component m_x can be compared with contrast due to m_y in the corresponding image below. Such contrasts are obtained experimentally, e.g., with the Kerr effect or Lorentz microscopy with differential phase contrast.

by experimental domain observations [12], [13] and *van den Berg's* theory for such elements [14], [15], we tried eight patterns for our study, six of which proved to be metastable at zero field.

Equilibrium states were obtained after numerical minimization of the total energy density consisting of anisotropy, exchange, and demagnetizing energy contributions

$$\epsilon_{\text{tot}} = \epsilon_k + \epsilon_x + \epsilon_d. \tag{1}$$

(Further details of the computational method are given in the Appendix, to which the interested reader is referred.) For each of the eight configurations, a pair of gray-shade images displays in Fig. 1 the magnetization components m_x and m_y along the in-plane directions for the parameters of SP1. Roughly, the configurations can be divided into two principal classes, which have either a low (Landau, diamond, tulip, and cross-tie states) or a high average magnetization and remanence (flower and C and S states). As we will demonstrate in Section IV, this classification corresponds to configurations that can be described by conventional, uniformly magnetized domain patterns, and more or less uniformly charged domains.

A. Investigation of the Requirements on Numerical Calculation

To determine the state of lowest energy, we at first studied the discretization requirements. According to our previous results [16], [17], one to two cells on the smaller one of the characteristic micromagnetic lengths $\sqrt{A/K_d}$ (the stray field exchange length) and $\sqrt{A/K_u}$ (the wall width parameter) was necessary to achieve mesh independence. For a soft magnetic material, such as in the case of SP1, $\sqrt{A/K_d}$ is the decisive length scale

that has to be described properly. Measured in these characteristic units, SP1 corresponds to $351.7 \times 175.8 \times 3.52$ units of the stray field exchange length. Expressed in discretization cells, this means that on a regular grid about $218\,000$ cells are necessary to have at least one cell per exchange length, and it takes 1.74 million cells to subdivide each characteristic length into two cells in every dimension. We had recently demonstrated the capability to calculate problems of this size using fast Fourier transform (FFT) techniques in our study of magnetic states in cube-shaped particles, [17] and could apply these methods in a straightforward manner to the present problem (we only used faster FFT routines that adapt to the specific architecture of the used computer [18]). To achieve mesh independence, we generally calculated all patterns on several meshes with decreasing cell size.

The convergence of the numerically calculated energies is plotted in Fig. 2 as a function of the inverse square of the number of discretization cells N along the long edge of the element. In Fig. 2(a), results for the lowest energy state (or "ground" state) of SP1 are shown. The variation between the grids $192 \times 96 \times 2$ and $768 \times 384 \times 8$, which is already below 1% is clearly insignificant for the decision that is the ground state when the four metastable domain states are compared in (b). To complete this example, the high-remanence states are included in (c) on a still larger energy scale. They are all energetically well above the domain states for this element size and geometry. In (b) and (c), the discretization $96 \times 48 \times 2$ (only one cell for every forth exchange length laterally) is included which, appears clearly insufficient.
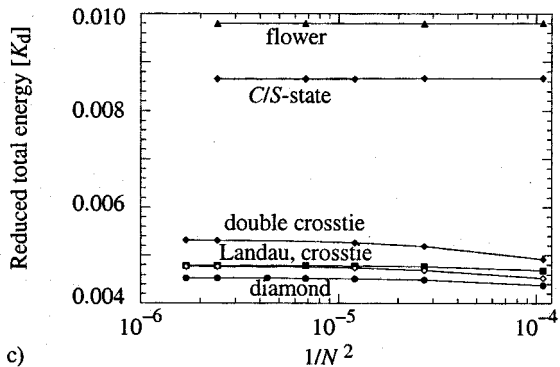
We note that for one to two cells per exchange length, the results become more or less independent of the mesh, confirming our expectations. Similarly we observed that the m_z-component
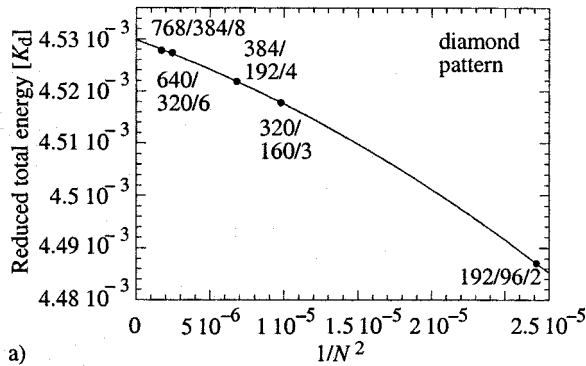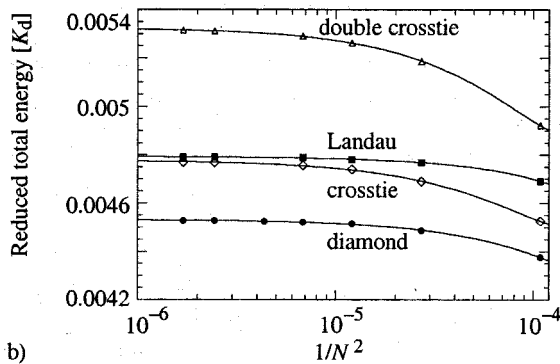
Fig. 2. Convergence of the total reduced energy of the investigated structures with the number of discretization cells N along the long edge of the element. (a) Only the diamond domain pattern is considered for several discretization levels. (b) Comparison of four domain patterns. (c) High-remanence states are included. Note the different energy scales.

in the vortex centers of the domain configurations needed discretization levels of one to two cells per stray field exchange length to approach unity, whereas for coarser grids, it was much reduced.

Due to the fact that the vortices were scarcely visible on the scale of Fig. 1 as tiny black and white dots in the m_z-component, we did not include these plots there. A comparison of the vortex evolution of the Landau structure at different sizes is intended to illustrate the relative importance of the central vortex (see Fig. 3; as throughout the rest of the paper, the element thickness is kept constant at 20 nm). The more or less continuously rotating structure at small sizes (a horizontal wall segment becomes only visible for $L = 0.5$ μm), in that the vortex is still
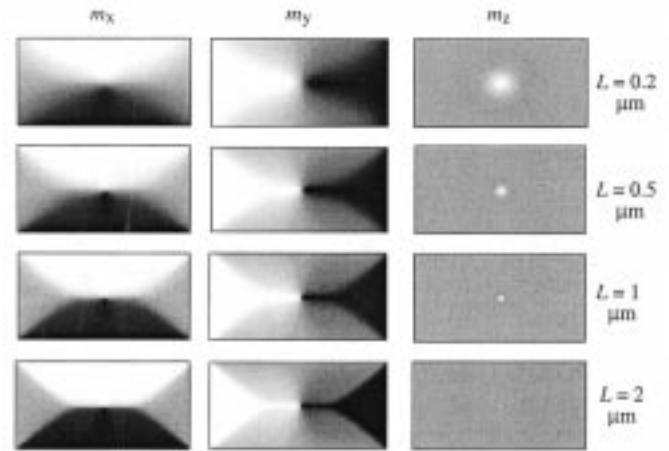

Fig. 3. Change of the Landau pattern with element size. Central vortex loses more and more importance with increasing element size. To resolve it correctly for $L = 2$ μm posed a challenge for SP1. Element thickness for all structures was kept at 20 nm.

a dominant part, transforms to a more or less regular domain pattern with increasing element size. On the scale of the parameters of SP1, the vortex is a tiny feature that becomes difficult to resolve properly.

From the energy variation between the grids in Fig. 2, we saw that the vortices do not contribute significantly to the total energy. However, such weak energy gradients cause stiffness problems in the energy minimization, because the vortex (vortices) can float around their optimum position(s). Therefore, we compared unconstrained calculations with others, where we kept the magnetization at the position of the vortex centers fixed, pointing along the vertical z-direction normal to the thin film. This constraint usually led to an acceleration by a factor of 5–10 in our energy minimization. In addition, it allowed us to compute the patterns at lower discretization without "losing" the m_z-component in the vortex centers.

Optimum vortex positions were obtained from several calculations with the vortices fixed at different positions along the long edge of the element, but always in the middle with respect to the short edge. The optimum for the Landau pattern was found at $L/2$, i.e, in the center of the element. The vortices of the diamond pattern have their optimum positions almost precisely at $L/4$ and $3L/4$, which is expected due to flux closure. For the cross-tie structures, values of $L/3$ and $2L/3$ are a good approximation. Precise values can be found in Fig. 4, where the energies of the different structures are plotted as a function of vortex position for the element sizes 2 μm $\times$ 1 μm (the benchmark parameters; compare the variation in energy in relation to Fig. 2) and 1 μm $\times$ 0.5 μm. The thickness was kept at 20 nm in both cases.

For sceptical readers, we mention that we compared, of course, some results with unconstrained calculations, but did not notice any significant difference to runs with the optimized positions beside longer computation time.

B. Results for the Parameters of the Standard Problem

Detailed results concerning the magnetic ground state of SP1 are collected in Table I, where the total reduced energy densi-
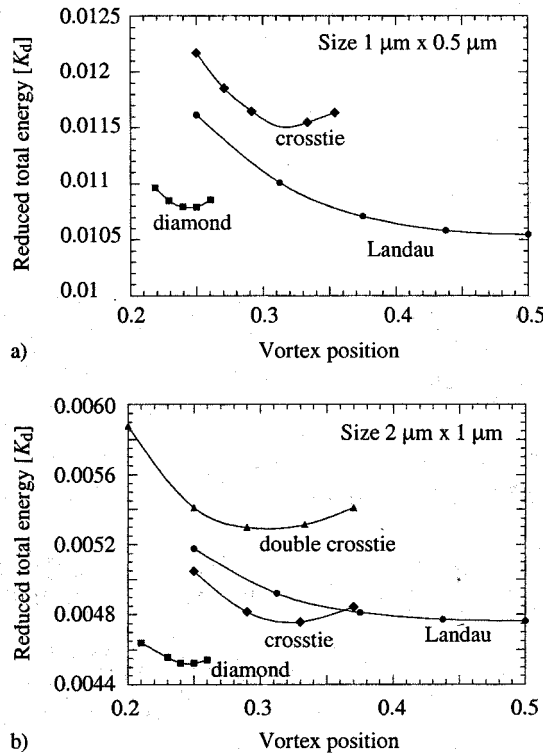
Fig. 4. Energy as function of fixed vortex position for (a) $L = 1\ \mu$m and (b) $L = 2\ \mu$m. Landau, diamond, single, and double cross-tie patterns were investigated (for $L = 1\ \mu$m, the double cross-tie is not yet stable and appears therefore not for this size).

TABLE I

EXTRAPOLATED TOTAL AND PARTIAL REDUCED ENERGY DENSITIES ϵ_i (DEMAGNETIZING, EXHANGE, AND ANISOTROPY) FOR THE STUDIED MAGNETIZATION PATTERNS WITH THE PARAMETERS OF THE STANDARD PROBLEM. ALL ENERGY DENSITIES ARE NORMALIZED WITH RESPECT TO THE STRAY FIELD ENERGY CONSTANT $K_d = \mu_0 M_s^2/2 = 3.9810^5\,\mathrm{J/m^3}$. FOR COMPARISON WITH OTHER RESULTS IN THE LITERATURE, THE TOTAL ENERGY e_{tot} IS GIVEN. IT IS RELATED TO ϵ_{tot} BY $e_{\mathrm{tot}} = \epsilon_{\mathrm{tot}} \times K_d \times V$ AND IS LISTED IN UNITS OF 10^{-17} J ($K_d \times V$ AMOUNTS TO 1.59×10^{-14} J FOR SP1)

Configuration	ϵ_{tot}	$\epsilon_d[K_d]$	$\epsilon_x[K_d]$	$\epsilon_k[K_d]$	e_{tot}
Flower	.00980	.00901	.00067	.00012	15.6
S-state	.00865	.00783	.00059	.00023	13.7
C-state	.00865	.00783	.00059	.00023	13.7
Landau	.00484	.00290	.00147	.00047	7.70
Diamond	**.00453**	.00193	.00198	.00063	**7.21**
single crosstie	.00476	.00220	.00210	.00045	7.57
double crosstie	.00532	.00214	.00276	.00042	8.46

ties with their different contributions (normalized to the stray field energy density K_d) are compared for seven different magnetic configurations. In addition, the total energy of the platelet in SI-units is specified. For this size, the high-remanence states have about twice as much energy as the domain patterns. Among the latter, the diamond structure represents the global energy minimum and saves about 5% in energy compared with the single cross-tie, and 6% in comparison with the Landau pattern, the two next favorable configurations. Although the flower state is probably not stable at this size (as will be explained in Sec-

tion III), we included its energies, which can be calculated using constrained vectors, for comparison.

For the tulip state for which we tried different variants (opening angle of the tulip, position of the tulip vortex), the situation was worse, because we could not find a pattern that did not decay finally into a diamond state for the sizes that we could investigate with sufficient discretization. The image displayed was obtained for a coarse grid of only one cell for every second exchange length $\sqrt{A/K_d}$. For this reason, we give no energies for the tulip pattern in Table I. Nevertheless, we kept the pattern in this paper, because the observation confirmed older assumptions [19], based on estimates of the associated domain and wall energies, that the experimentally well-known tulip configuration is stabilized only extrinsically, i.e., by defects to which the additional vortex in the interior might attach or edge roughness where the two edge singularities (there are two points where the magnetization has to point out of, or into, the element) can be pinned.

III. SIZE DEPENDENCE OF THE GROUND STATE CONFIGURATION

In order to find out what kind of domain patterns might occur in even larger elements, and when quasi-single-domain states with high remanence would become absolutely stable at smaller sizes, we extended the previous calculations to different element sizes. Keeping the thickness of 20 nm, the other material parameters as well as the aspect ratio of $2:1$ unchanged, we varied only the length of the element. The calculated size dependence of the reduced total energies of the different structures is displayed in Fig. 5. The reduced total energy density normalized to the stray field energy density of the five configurations with lowest energy for element sizes up to two microns is shown in (a). These curves, which can be immediately correlated with an effective demagnetizing factor (demagnetizing factors for the circumscribed and inscribed ellipsoids are 0.0044 and 0.0062, respectively) and are difficult to tell apart, however. Therefore, we plot in (b) and (c) the product of reduced energy density times reduced length, as a function of the element length in micrometer. This makes the transition points more distinguishable. Starting at small sizes [Fig. 5(b)], a first transition from the flower to the C and S states occurs slightly above $L = 100$ nm. The transition is caused by a gain in stray field energy at larger sizes, corresponding to a second-order phase transition that is similar to a kind of "buckling" (the term should be used with care and not be confused with the eigenmode of ellipsoids, of course). The critical length can be determined by monitoring the magnetization vectors at the center of the end faces of the elements (the vectors are indicated in the inset in Fig. 6). The m_y-component of these vectors is plotted as a function of element size for the S and C states in Fig. 6. It vanishes at about 105 nm for the C state and at about 110 nm for the S state. This means that the C state remains stable for smaller particles and is thus slightly favored relative to the S state. (An oblique external field on the other hand, would select an S state that can provide a higher moment in field direction.)

Above the transition from the flower to the C and S states, the flower state should obviously be instable and decay into either
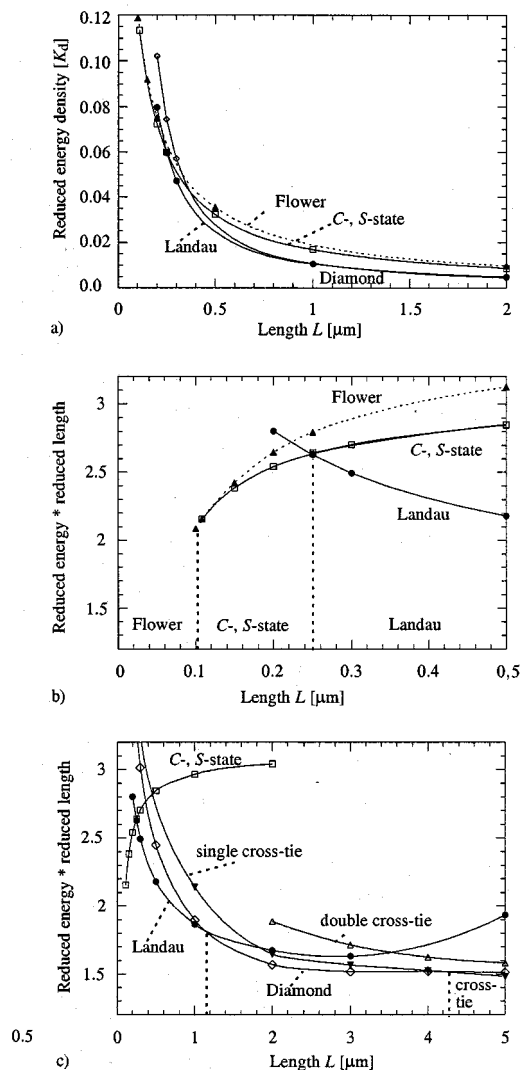
Fig. 5. Size dependence of the total reduced energy of the seven considered configurations as a function of edge length L. (a) Results show the reduced energy density for the configurations as a function of element length up to 2 μm. (b) and (c) Product of reduced energy and reduced length is plotted against edge length for better distinction between the curves. Replacement of the flower by the C state and then by the Landau state, which marks the transition from high-remanence to domain states is shown in (b). Further transitions of the ground state from the Landau to the diamond and the single cross-tie pattern were found for increasing element size (c).

Fig. 6. Determination of the critical element sizes for which the flower state is replaced by the C- or S state. Transition to the C state occurs slightly earlier.

one of the former configurations. This is the reason for plotting the energy curve of the flower state with a dashed line.[2]

The first low-remanence domain state that becomes favorable with increasing element size is the Landau pattern at about $L =$ 250 nm. This might be expected, because it consists of only four domains that can efficiently close the flux and the total wall length is small. The reason why this configuration gets again replaced by another, energetically more favorable one at larger element sizes, is the existence of a 180° wall segment that has a much higher energy in thin films than, e.g., 90° walls, where the dipolar energy is reduced due to the smaller wall angle.

To make this qualitative argument more precise, we calculated the energies and wall profiles of 180° and 90° symmetric Néel walls in infinitely extended thin films (see Fig. 7). This was done for SP1 parameters using the method developed by Riedel and Seeger [20]. The transition from symmetric to asymmetric Néel walls should occur clearly above the thickness of SP1 (see, e.g., [21]). Essential is the strong dependence of wall energy ϵ_w on wall angle Ω_w, predicted already by Néel [22] to

$$\epsilon_{w(\Omega_w)} = \epsilon_{w(180°)} \times [1 - \cos(\Omega_w/2)]^2. \qquad (2)$$

With a fit to the energy of the 180° wall, this formula is a very good approximation. We also note that the extension of the logarithmic tail of the wall amounts to about 10 μm. This can be estimated for general material parameters using $W_{\text{tail}} = 0.56\, D/Q$ [23] and means that we clearly deal with interacting Néel walls in these thin-film elements.

Returning to Fig. 5, we notice that at about 1.1 μm, the Landau pattern is replaced as the ground state by the diamond structure, which possesses only 90° walls. At still larger sizes, the more complicated cross-tie patterns take over, which achieve a further reduction in energy due to the reduced total length of 90° walls. For our parameters, this occurs at about $L = 4.3\ \mu$m. Our algorithm and our equipment reached their limit at a length of about $L \approx 5\ \mu$m. Therefore, a further ground state transition from the single cross-tie to the double cross-tie pattern (which might occur at about $L \approx 8\ \mu$m) could not be confirmed.

IV. DOMAIN MODELS FOR THE METASTABLE STATES

Analyzing the investigated patterns using domain models allows us to understand the mechanisms leading to their formation. In addition, it makes it possible to check efficiently wider parameter ranges and extrapolate to sizes that are not accessible to micromagnetic computations. Therefore, such models were

---

[2]We investigated the possibility of whether the flower state could become metastable again for larger sizes, due to a small energy barrier separating it in configuration space from the C and S configurations. To answer this question, we used constrained calculations, where we assigned fixed in-plane directions to the same two vectors in the center of the end faces, which we had monitored in Fig. 6 as a function of element size. Rotating these vectors systematically, to induce the "buckling" symmetry of the C state, we calculated the energy as a function of rotation angle. For different element sizes up to $L = 2\ \mu$m, we always observed an energy decrease with increasing rotation angle. Therefore, no indication for metastability at larger sizes was seen. The calculated energy decrease for a given rotation angle (values of 10^{-30} J for a rotation angle of 0.5° were typical) became smaller with increasing size, however, indicating that a small defect could stabilize the flower state by pinning.
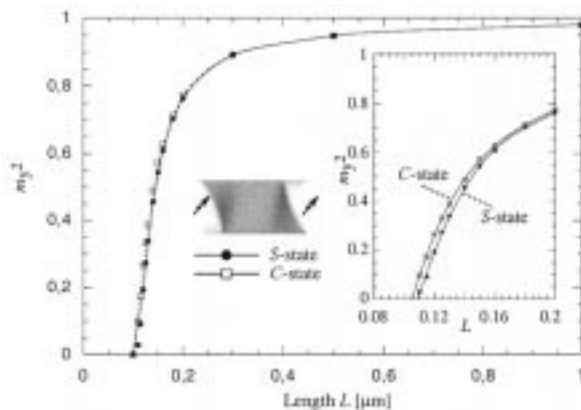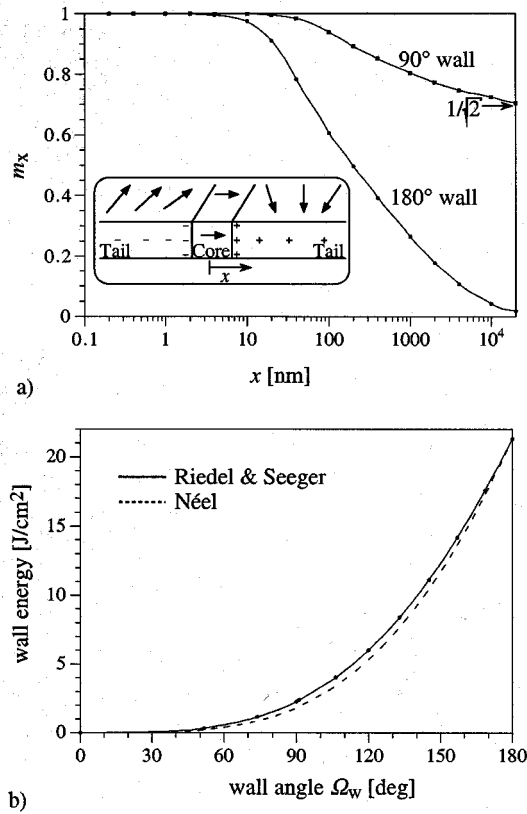
a)

b)

Fig. 7. (a) Wall profiles for symmetric 90° and 180° Néel walls calculated with the method of Riedel and Seeger for the parameters of SP1 in an infinitely extended thin film. (b) Corresponding variation of the wall energies as a function of wall angle. Comparison with Néel's simple original model is included.

Fig. 8. (a) Locus of a charge free wall for the C or S state. Magnetization in the longitudinal domain is assumed to be oriented horizontally. (b) Domain model, where in addition a rotation segment in two corners was assumed. (c) Magnetization maps of the m_y-component with energies connected to the model are indicated with and without averaging using a Gaussian filter.

The condition for a charge-free wall is simply

$$\mathbf{m}_1 \cdot \mathbf{n} = \mathbf{m}_2 \cdot \mathbf{n} \qquad (3)$$

where $\mathbf{m}_1$ and $\mathbf{m}_2$ represent the magnetization directions in the two domains and $\mathbf{n}$ is the wall normal. If the x-component of the magnetization in the edge domain increases linearly with the x-coordinate as $m_x = x/a$, this condition reads as

$$\frac{1}{a}\left(\frac{x}{\sqrt{a^2 - x^2}}\right) \cdot \begin{pmatrix} -y_c' \\ 1 \end{pmatrix} = \begin{pmatrix} 1 \\ 0 \end{pmatrix} \cdot \begin{pmatrix} -y_c' \\ 1 \end{pmatrix} \qquad (4)$$

leading to a differential equation for the curve describing the locus $y_{c(x)}$ of the wall of the C state

$$\frac{dy_c}{dx} = y_c' = -\sqrt{\frac{a+x}{a-x}}. \qquad (5)$$

The integration constant follows from the condition that the wall position at $y = 0$ has to be $x = a$

$$y_{c(x)} = -\sqrt{\frac{a+x}{a-x}} - a\arcsin\frac{x}{a} + \frac{\pi a}{2}. \qquad (6)$$

The other boundary condition at the opposite end of the short edge $x = 0$ for $y = 0$ determines the extension a of the edge domain in terms of the width W of the thin-film element

$$a = \frac{2}{2 + \pi} W. \qquad (7)$$

In this way, the form of the walls observed experimentally as well as in our micromagnetic simulations follows naturally.

We refined the domain model by adding rotation segments of the magnetization in those two corners, where again charges would be created by a magnetization meeting bluntly the long edge and by smoothing the magnetization pattern with a Gaussian filter according to

$$\overline{m} = \frac{\sum_{i,j} m_{i,j} \exp(-\kappa r_{i,j})}{\sum_{i,j} \exp(-\kappa r_{i,j})}. \qquad (8)$$

intended to serve as a link between micromagnetics and domain theory, as outlined, e.g., in [21] in the context of closure domains.

The low-remanence states (with the exception of the Landau state, as we will demonstrate below) can be modeled fairly precisely by regular constant-magnetization domains. These domains are separated by low-angle Néel walls, which distribute their charges to some extent into the neighboring domains. For this reason, weak, more or less uniform charges are present in almost all domains, in contrast to domain patterns in bulk material. Characteristic for the high-remanence states, however, is the formation of *strongly* charged domains.

As examples, we concentrate on domain models for two states that emphasize the importance of charged domains: the C state and the Landau state. The features of these configurations can be derived from the fact that the stray field energy is reduced efficiently, if the charges are uniformly distributed.

A. Domain Model for the C State

This underlying principle of uniform charge distribution becomes evident, if we try to construct a charge-free wall that separates the edge-domain of a thin-film element from the basic domain, which is assumed to be magnetized along the long edge (see sketch of the domain model for the C state in Fig. 8).
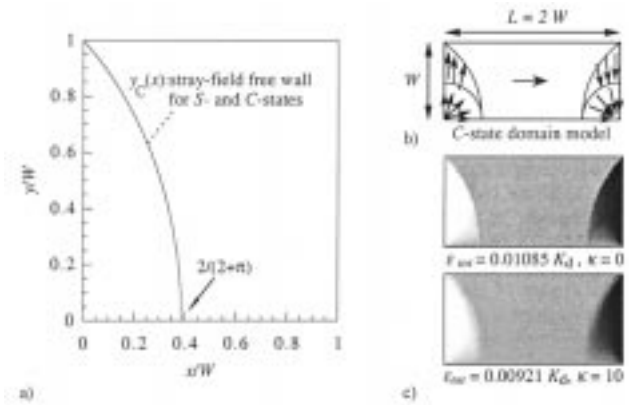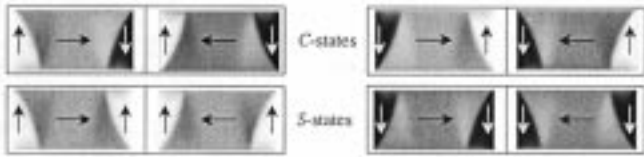
Fig. 9. Equivalent degenerate configurations for the C and S states. States are grouped according to conservation of the magnetization along the short edges as expected for hysteresis loops with a field along the long edge.

The parameter κ is counted in units of the inverse exchange length $\sqrt{A/K_d}$. Two patterns (with and without the smoothing operation) prepared according to this recipe are shown in Fig. 8. Optimization of the smoothing parameter leads on a coarse grid of $96 \times 48 \times 2$ cells to an energy that is only about 6% above the one obtained by numerical energy minimization. This means that with much less numerical effort, a realistic estimate for the energy is obtained.

From the necessity of charge-free walls, also the four equivalent states for the C and S configurations follow naturally. They are depicted in Fig. 9, grouped according to conservation of the magnetization along the short edge of the element. This would be expected for magnetization loops in a field parallel to the long edge.

Similarly in the flower state, two (instead of one) edge domains are formed, occupying each only half of the element width and extending therefore only half as wide into the element, namely, $(1/(2+\pi))W$. This leads to a slightly higher remanence, making the flower state the preferred configuration in high fields parallel to the long edge.

B. Domain Model for the Landau Pattern

In a similar manner, the Landau pattern can be analyzed. Here, the central 180°-Néel wall has about 9.5 times as much energy than does a 90° wall (compare with Fig. 7). A reduction of the wall angle accompanied by a charge distribution could again be achieved by a linear variation of the magnetization direction, this time in the domains along the long edge of the element. The same reasoning as outlined above is applied, this time with the closure domain magnetized homogeneously along y and allowing a linear variation of m_y in the longitudinal domains. Under this assumption, the locus of the wall (the x-coordinate in terms of y) can be determined to

$$x_{L(y)} = \left[\arcsin \beta y - \sqrt{1 - \beta^2 y^2} + 1 \right] \Big/ \beta. \qquad (9)$$

One free parameter β remains that describes the maximum value of m_y at the wall separating the longitudinal domains (for the C state, the parameter was simply one). Calculated wall curves for different values of this parameter are shown in Fig. 10.

The optimum value for β with SP1-parameters was found by minimizing the energy of an accordingly constructed domain model with respect to β on a grid of $96 \times 48 \times 2$ cells. We obtained $\beta \sim 0.59$, corresponding to a vertex position at about $1.396 \times W/2$ (instead of just $W/2$) and a wall angle of $\sim 145°$ instead of 180°. This means already only about one-half of the wall energy.
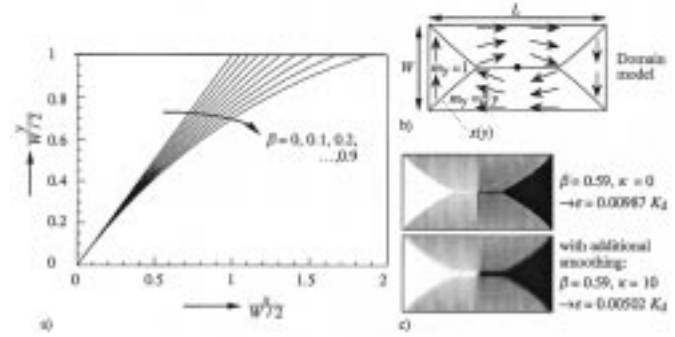

Fig. 10. (a) Locus of charge-free walls between an exactly vertically magnetized closure domain and a longitudinal domain in which the magnetization is allowed to rotate linearly away from the horizontal edge. Different amounts of maximum rotation leading to different reductions of the 180° wall angle are compared. (b) Domain model of the whole element is sketched, of which (a) represents the lower left quarter. (c) Configurations and energies connected with this model, with and without averaging using a Gaussian filter.

This result for the domain model of the Landau pattern should be contrasted with the energy for a diamond pattern, which we obtained by a simple arrangement of 90° walls, i.e., without allowing charges in the domains (corresponding to $\beta = 0$ in terms of the model for the Landau pattern). Orienting the magnetization along the four [100]-directions and again using a Gaussian filter to smooth the wall transitions appropriately, we found an optimized energy of $\epsilon_{\text{tot}} = 0.00515 K_d$. Although a model with $\beta = 0$ for the Landau pattern yields results 50–60% above the correct result, this is already within 12% of the result after numerical relaxation, demonstrating again the large (energy) difference between 90° and 180° walls.

C. Charge Distributions of the Investigated Patterns

To check the validity of our domain models using charged domains, we compared the charge patterns of the investigated domain structures. These charge patterns are also expected to be seen in MFM observations [24], [25], if tip sample interactions are not dominating the contrast.

For all eight different patterns, we display in Fig. 11 the magnetic flux entering a column of our discretization grid oriented along the z-direction (the smallest dimension of the platelet). This quantity, which is a function of the in-plane coordinates x and y, is proportional to the magnetic surface charges plus the averaged volume charges over the z-direction

$$\phi_{(x, y)} = \iint \mathbf{m}_{(x, y, z)} \cdot \mathbf{n} \, dS \propto \overline{\rho}_{(x, y)}. \qquad (10)$$

For all patterns, the contrast was enhanced with the same grayscale transformation $f(x) = \tanh(\operatorname{arctanh}(10\times))$ to bring out the characteristic features more clearly.

The description of the high-remanence states by charge domains appears to be at least a good approximation. In the low-remanence configurations, the charge concentration in the 180° wall of the Landau state and the corresponding reduction in the 90° walls of the diamond configuration become visible. The continuation of the game, to distribute charges at the expense
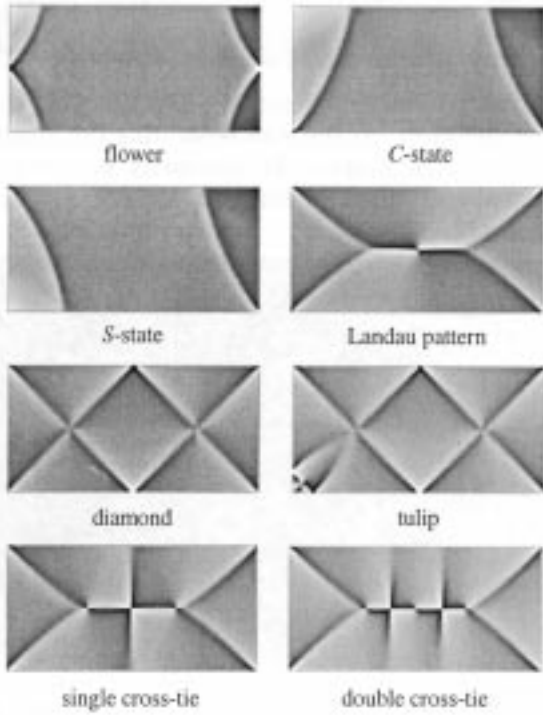
Fig. 11. Charge patterns of the investigated configurations displayed with equivalent contrast. Element size is $L = 2\,\mu$m. Although Fig. 1 presented a contrast expected for Kerr or Lorentz microscopy, the above images could be observed with magnetic force microscopy.

of a minimum amount of wall length, can be followed in the cross-tie structures.

V. CONCLUSION

The investigation of the energies of possible magnetization patterns in a rectangular thin-film element revealed that at least five different "ground" states are possible for varying element sizes with a thickness supporting symmetrical Néel walls: starting at small sizes, and increasing the size, we found flower, C, Landau, diamond, and single cross-tie states. Multiple cross-ties are expected for larger elements making the connection to extended thin films of this thickness.

The sequence of patterns as a function of size can and will be modified for different film thickness, because in thicker films, supporting asymmetric Néel and Bloch walls, no cross-tie walls will be found any more.

The rectangular shape has to be made rather small to make a high remanence state absolutely stable. Uniformly charged domain patterns can fairly well describe structures with such a high magnetic moment. Appropriately curved walls are a signature of these configurations, which will also explain features observed in applied fields, such as the concertina pattern.

APPENDIX I
MICROMAGNETIC METHOD

As stated in (1), the normalized total magnetic energy per volume was calculated, taking into account uniaxial anisotropy, exchange, and demagnetizing energy contributions

$$\epsilon_{\text{tot}} = \frac{e_{\text{tot}}}{K_d V} = \epsilon_x + \epsilon_k + \epsilon_d. \tag{11}$$

Using the gradient of this energy density, the "effective field"

$$\mathbf{H}_{\text{eff}}(\mathbf{r}) = -\frac{1}{\mathbf{J_s}} \frac{\delta\epsilon_{\text{tot}}}{\delta\mathbf{m(r)}} \tag{12}$$

obtained by differentiating the total energy density with respect to the local magnetization $\mathbf{m(r)}$, was minimized. To this end, an iteration algorithm that alternatingly performs some (small) relaxation steps in the direction opposite to the local effective field and then, after several successful such steps, tries to perform a large step by a complete function minimization with respect to the present gradient direction, was applied [26], [27].

The method can be viewed as a way of solving the Landau–Lifshitz equation without the precession term but with an adaptive relaxation coefficient α_D, as first described in [28]. An iteration step was performed according to

$$\mathbf{m}^{\text{new}} = \mathbf{m}^{\text{old}} - \alpha_{\mathbf{D}}[\mathbf{m}^{\text{old}} \times (\mathbf{m}^{\text{old}} \times \mathbf{H}_{\text{eff}})] \tag{13}$$

until the component of the effective field perpendicular to the magnetization was everywhere smaller than a certain fraction of the anisotropy field $H_k = 2\,K_u/J_s$. This fraction was taken between 10^{-3} and 10^{-2}.

Although the local energy terms of anisotropy and exchange are easily calculated, the demagnetizing field term together with the energy minimization are the critical parts in solving most micromagnetic problems.

Our algorithm to calculate the demagnetizing energy and demagnetizing field is the generalization of the method published in [29] from two-dimensional (2-D) to three-dimensional (3-D). At first, we determine volume and surface charges according to

$$\rho = -\nabla \cdot \mathbf{m}; \qquad \sigma = \mathbf{m} \cdot \mathbf{n} \tag{14}$$

with $\mathbf{n}$ being the outward surface normal. Knowing the charges, the scalar potential of the demagnetizing field is given by

$$\phi(\mathbf{r}) = \frac{J_s}{4\pi\mu_0} \left(\int_{V'} \frac{\rho(\mathbf{r'})}{|\mathbf{r} - \mathbf{r'}|}\, \mathbf{dV'} + \int_{S'} \frac{\sigma(\mathbf{r'})}{|\mathbf{r} - \mathbf{r'}|}\, \mathbf{dS'} \right) \tag{15}$$

which leads to the six-fold integral for the stray field energy

$$\epsilon_D = \frac{J_s^2}{4\pi\mu_0} \left(\int_{V'} \rho(\mathbf{r'})\phi(\mathbf{r'})\, \mathbf{dV'} + \int_{S'} \sigma(\mathbf{r'})\phi(\mathbf{r'})\, \mathbf{dS'} \right). \tag{16}$$

Numerically, these standard expressions are approximated by subdividing the computational region into $L \times M \times N$ parallelepipeds (we also use the terms cells or finite elements). Magnetization vectors in the corners of the cells are assumed, and averaged potential values over their volumes and surfaces are calculated (see sketch in Fig. 12). For the potential in the interior, we end with cell–cell and cell–surface interactions, whereas for the potential values on the bounding surfaces, cell–surface and surface–surface interactions have to be evaluated. All necessary integrations for the interactions between charged volume and (differently oriented) surface elements can be carried out analytically. In this respect, the present approach might be traced back to [30]. The precise analytical expressions we use can be found in [21, pp. 123–124]. Here, it may suffice to say that we denote the interaction coefficients by W^{222}, W^{221}, W^{220}, etc., where the indexes represent the number of integrations along x, y, and z.
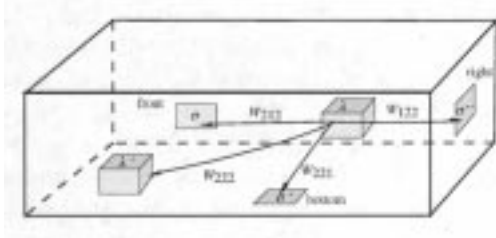
Fig. 12. Surface and volume charges of the parallelepipeds subdividing the computational region. Interactions among these charges are indicated schematically.

Due to the three possible orientations of the surface elements, four sums arise. For example, the potential values in the interior of the cells are thus written as

$$\phi_{i,j,k}^{\text{vol}} = \frac{J_s}{4\pi\mu_0}\left(\sum_{l,m,n}^{L,M,N} \rho_{l,m,n} W_{|i-l|,|j-m|,|k-n|}^{222}\right.$$
$$+ \sum_{l,m}^{L,M} \sigma_{l,m}^{\text{bot}} W_{|i-l|,|j-m|,k}^{221}$$
$$+ \sigma_{l,m}^{\text{top}} W_{|i-l|,|j-m|,N+1-k}^{221}$$
$$+ \sum_{l,n}^{L,N} \sigma_{l,n}^{\text{front}} W_{|i-l|,j,|k-n|}^{212}$$
$$+ \sigma_{l,n}^{\text{back}} W_{|i-l|,M+1-j,|k-n|}^{212}$$
$$+ \sum_{m,n}^{M,N} \sigma_{m,n}^{\text{left}} W_{i,|j-m|,|k-n|}^{122}$$
$$\left.+ \sigma_{m,n}^{\text{right}} W_{L+1-i,|j-m|,|k-n|}^{122}\right). \quad (17)$$

The surface charges on the different bounding surfaces of the computational region are denoted by σ_{bot}, σ_{front}, σ_{left}, etc. On the bottom side of the computational region, the surface potential is calculated by

$$\phi_{i,j}^{\text{bot}} = \frac{J_s}{4\pi\mu_0}\left(\sum_{l,m,n}^{L,M,N} \rho_{l,m,n} W_{|i-l|,|j-m|,n}^{221}\right.$$
$$+ \sum_{l,m}^{L,M} \sigma_{l,m}^{\text{bot}} W_{|i-l|,|j-m|,0}^{220}$$
$$+ \sigma_{l,m}^{\text{top}} W_{|i-l|,|j-m|,N}^{220}$$
$$+ \sum_{l,n}^{L,N} \sigma_{l,n}^{\text{front}} W_{|i-l|,j,n}^{211}$$
$$+ \sigma_{l,n}^{\text{back}} W_{|i-l|,M+1-j,n}^{211}$$
$$+ \sum_{m,n}^{M,N} \sigma_{m,n}^{\text{left}} W_{i,|j-m|,n}^{121}$$
$$\left.+ \sigma_{m,n}^{\text{right}} W_{L+1-i,|j-m|,n}^{121}\right). \quad (18)$$

Analogous expressions exist for the other surfaces. To compute these expressions in an acceptable time, the Fourier transform is applied, which cuts the computation time down from the order $O((L \times M \times N)^2)$ to $O(L \times M \times N \log(L \times M \times N))$. With proper zero padding, the convolution theorem can be exploited [31]. For the example of the potential values in the interior (17), the following transforms are required (Fourier transformed quantities are marked by a tilde sign in the following, the convolution in real space is represented by the symbol $*$):

$$\rho * W^{222} \quad \overrightarrow{\text{FFT}_{xyz}^{3\text{D}}} \quad \tilde{\rho} \cdot \tilde{W}^{222}$$

$$\sigma_{\text{bot}} \sigma_{\text{top}} * W^{221} \quad \overrightarrow{\text{FFT}_{xy}^{2\text{D}}} \quad \tilde{\sigma}_{\text{bot}} \cdot \tilde{W}^{221}, \tilde{\sigma}_{\text{top}} \cdot \tilde{W}^{221}$$

$$\sigma_{\text{front}} \sigma_{\text{back}} * W^{212} \quad \overrightarrow{\text{FFT}_{xz}^{2\text{D}}} \quad \tilde{\sigma}_{\text{front}} \cdot \tilde{W}^{212} \tilde{\sigma}_{\text{back}} \cdot \tilde{W}^{212}$$

$$\sigma_{\text{left}} \sigma_{\text{right}} * W^{122} \quad \overrightarrow{\text{FFT}_{yz}^{2\text{D}}} \quad \tilde{\sigma}_{\text{left}} \cdot \tilde{W}^{122} \tilde{\sigma}_{\text{right}} \cdot \tilde{W}^{122}. \quad (19)$$

The Fourier-transformed potential contributions are summed in the frequency domain

$$\tilde{\phi}_{i,j,k} = \tilde{\rho} \cdot \tilde{W}^{222}$$
$$+ \tilde{\sigma}_{\text{bot}} \cdot \tilde{W}^{221} + \tilde{\sigma}_{\text{top}} \cdot \tilde{W}^{221}$$
$$+ \tilde{\sigma}_{\text{front}} \cdot \tilde{W}^{212} + \tilde{\sigma}_{\text{back}} \cdot \tilde{W}^{212}$$
$$+ \tilde{\sigma}_{\text{left}} \cdot \tilde{W}^{122} + \tilde{\sigma}_{\text{right}} \cdot \tilde{W}^{122} \quad (20)$$

and transformed back to the spatial domain

$$\tilde{\phi}_{i,j,k} \quad \overrightarrow{\text{inv.FFT}_{xyz}^{3\text{D}}} \quad \phi_{i,j,k}. \quad (21)$$

The algorithm is further accelerated by the application of Parseval's theorem when performing energy minimizations in the relaxation algorithm for which the backward transform of the potential is not needed, because the effective field is only required for the finally executed iteration step.

An additional factor of about 2 is gained by combining Fourier transforms of different potential contributions or using intermediate results of quantities to be transformed in several dimensions. This takes advantage of the linearity of the Fourier transform and is the reason why we use one-dimensional (1-D) FFT routines. As an example, consider the 3-D FFT transformation of the volume charges (see Fig. 13). These are needed for the potential in the interior of the cells, but the intermediate result after two transforms can be used already to compute a part of the surface potential, say, on the xy-surfaces. Thus, N 2-D-transforms of size $2L \times 2M$ are saved, if the data array can be accessed at that stage. Similarly, 2-D-transformed slices of the array of volume charges ρ are needed for the potential values on the other surfaces in combination with the interaction coefficients W^{212} and W^{122}. In this case, first the common transform along z is performed, which is taken as the starting point for the following transformations along x and y [see Fig. 13(b)]. In an analogous way, the inverse transform of the potential can be arranged. As schematically sketched in Fig. 13(c), the common transforms along x and y of the potential contributions due to volume and xy-surface charges and the common transform along z of the contributions of the xz- yz-surface charges are performed together. For the potentials on the surfaces, which also consist of four terms each, additional possibilities were exploited to combine transforms in the forward as well as in the backward direction.
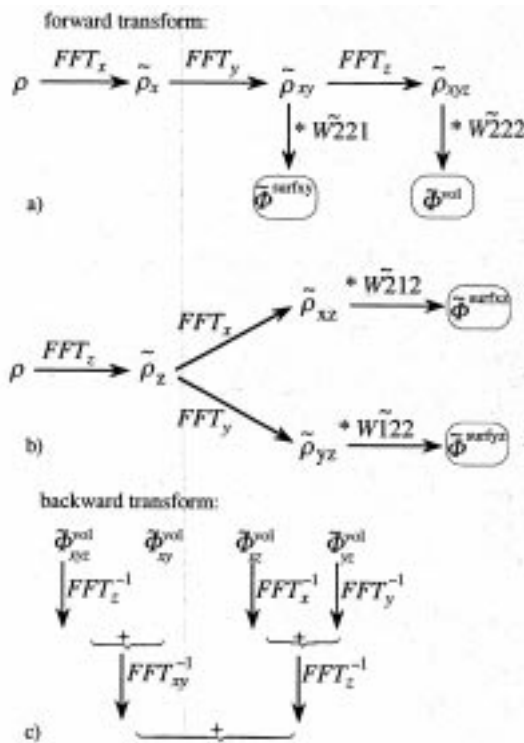
Fig. 13. Common FFT transforms of different potential contributions: (a) Volume charges ρ, transformed along x and y, can be used to calculate the potential contribution on the xy-surfaces before the transform along z leads to the contribution to the volume potential. (b) Intermediate result of the volume charges transformed along z is used for both potential contributions on the xz and yz surfaces. (c) Backward transform of the potential in the interior combines common transforms along x and y of the contributions due to volume and xy-surface charges and common transform along z of the contributions due to xz- and yz-surface charges.
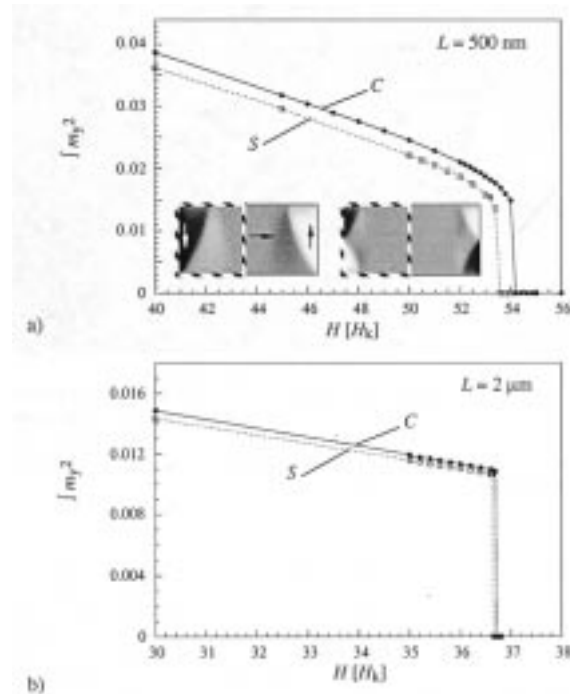

Fig. 14. Transition from the C or S state to the flower state in an applied field along the long edge of the sample for the element sizes (a) $L = 500$ nm and (b) $L = 2\,\mu$m. Boxes in the magnetization maps indicate the zone of integration of the m_y-component.

APPENDIX II
SWITCHING FIELDS

Having investigated the zero-field state, we were of course also interested in the switching behavior of such rectangular thin-film elements. In determining the switching fields, we focused on the simple case of a field aligned exactly parallel to the long particle axis. In high positive fields, the approach to saturation must occur in the symmetry of the flower state due to its larger magnetic moment along the long edge compared with the C and S states. Reducing the field, there had to be a point at which the flower state becomes unstable. For positive fields, this marks a continuous symmetry breaking into the C state; otherwise, we expected a discontinuous switching into a near-saturation state of opposite polarity. Depending on the exact field history, one or the other of these states should form the starting configuration for magnetization reversal. As stated before (13), we studied these switching processes in the limit of infinite damping, without taking into account the precession term of the Landau–Lifshitz-equation. All three switching points, that of the flower, the C state, and the S state depend on particle size and were investigated for two sizes, $L = 500$ nm and $L = 2\,\mu$m, to get an idea of the switching fields and identify the possible switching modes.

A. Transitions Coming from High Positive Fields

We first tried to determine which branch of the solution is relevant coming from high fields. The expected second-order transition from the flower configuration into the S- or C state was studied, exploiting the integral value of the m_y-component as the order parameter. Computing this parameter in half of the element (in the C state, a cancellation would occur due to another mirror symmetry), gives a convenient measure for the decay of the S or C states in an applied field.

This is demonstrated in Fig. 14 for the C and S states, which will be nucleated coming from high fields already at a positive field of approximately 54 H_k for $L = 500$ nm or at about 37 H_k for $L = 2\,\mu$m (the value of H_k is 12.5 Oe or about 1000 A/m for our parameters).

The transition fields for the S states are slightly smaller, again showing that the C states are marginally preferred. The differences decrease with size, however, indicating that both patterns are nearly degenerate in practice. As mentioned before, this degeneracy can be lifted in oblique fields, leading to the selection of an S state, but a conversion will only happen if the field was high enough, because the edge magnetization is conserved during reversal (it takes place either from a C- to another C- or from an S- to another S-configuration).

Because the occurrence of the S state seemed clearly possible, we decided to investigate the reversal of both C and S states for which hysteresis loops for the smaller size of $L = 500$ nm are shown in Fig. 15.

B. Switching of a Small Element with $L = 500$ nm

Finer details of the demagnetization curves can be seen in Fig. 16. In the C-configuration, two irreversible events are
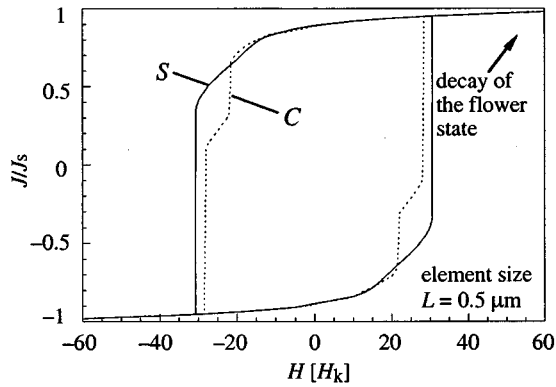
Fig. 15. Hysteresis loops for the high-remanence states and an element size $L = 500$ nm in a field applied along the long edge. Transition from the flower to the C state occurs at $\simeq 54 \; H_k$. Due to the near degeneracy of the C and S states, both loops after this first branching process are displayed.

clearly discernible. First, at about $H = -22 \; H_k$, the edge domains expand, destroying a faintly developing concertina pattern and creating a vertical $180°$ wall segment between them. In a second step, the final reversal takes place initiated for this element size close to the lower two corners.

A different reversal mechanism is observed for the S state. Here, the growth of the edge domains leads to the formation of a third domain, interconnecting them. This probably irreversible process shows weakly up in the magnetization curve by a slight "bump." The curved domain walls between this inner domain and the edge domains contain the nuclei for the complete reversal of the element.

The reversal mechanisms were deduced from the evaluation of the susceptibility. As outlined in detail in [32], the switching event is almost always "announced" before the actual irreversibility by the divergence of the reversible susceptibility in the switching nucleus. Extrapolation of the inverse square of this susceptibility (see Fig. 17) can thus circumvent the difficulty to calculate a field corresponding to a nonequilibrium state (our, and practically all other, micromagnetic programs are designed to calculate equilibrium states). The susceptibility was defined by

$$\chi^2 = \frac{\Delta m_x^2 + \Delta m_y^2 + \Delta m_z^2}{\Delta h^2} \qquad (22)$$

and evaluated in a region extending three to four times $\sqrt{A/K_d}$ around the position that showed the highest values in the thin-film element (displayed as dark regions in the susceptibility maps of Fig. 17; they are derived from the last two stable computed states before the "observed" switching event). Grid independence was again achieved at about one to two cells per exchange length $\sqrt{A/K_d}$ for a problem size corresponding to about $(88 \times 44) \; A/K_d$.

For the C state, a still finer discretization with $256 \times 128 \times 4$ cells was tried, because a different switching mode was found for $L = 2 \; \mu$m, but the result remained unchanged. The other region with high susceptibility in this configuration at the top middle could not well be extrapolated. For the S state, the total susceptibility was also a good measure. The diverging susceptibility becomes also visible in the increasing slope of the magnetization curve. As mentioned in Section IV, the reversal mech-
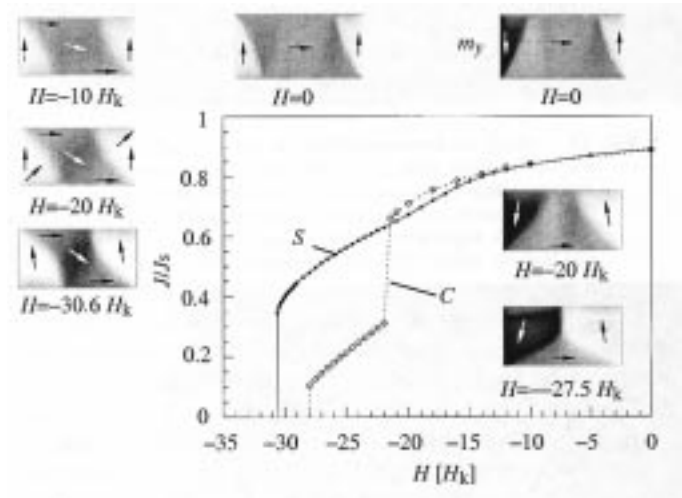

Fig. 16. Second quadrant of the hysteresis loops in Fig. 15. Demagnetization curves for C and S configurations for the element size $L = 500$ nm are displayed with m_y-magnetization maps for several characteristical field values to visualize the reversal modes. To guide the eye, a few vectors are inserted to indicate the general magnetization direction.
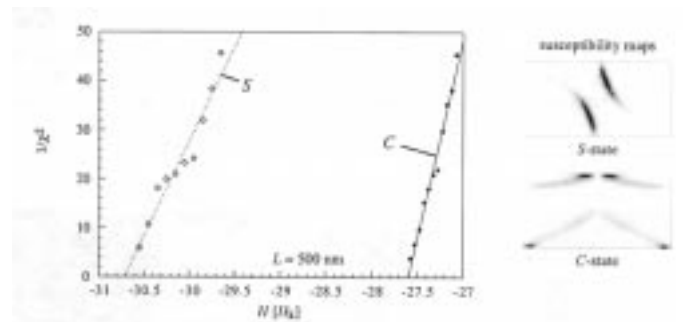

Fig. 17. Study of irreversibilities in the C and S configurations for the element size $L = 500$ nm. Square of the inverse susceptibility is extrapolated to zero to derive the switching field. Nucleation modes are visualized by maps of the susceptibility, where dark regions mark the areas, where this quantities shows the highest values. Discretization used was $192 \times 96 \times 2$ cells.

anisms conserve the magnetization orientation along the short edges and the final states are of the same type as the starting configurations. The shape of the walls of the edge domains has to be inverted to create again charge-free walls compatible with the inverted interior magnetization.

C. Switching of an Element with the Benchmark Parameters

Due to the fact that we could not unambiguously clarify the magnetization reversal for this size, we did not put our results concerning the hysteresis properties in the regular part of the paper. Nevertheless, we observed some features that were interesting enough to serve as a starting point for further investigations.

The demagnetization curves for the C and S states for $L = 2 \; \mu$m are presented in Fig. 18. Compared with $L = 500$ nm, a more pronounced development of the concertina pattern leads to distinct jumps in both configurations when the edge domains interconnect. The development for the S state was similar to the one observed for $L = 500$ nm (see Fig. 19). After a first irreversible magnetization jump at $h = -3.9 \; H_k$, where
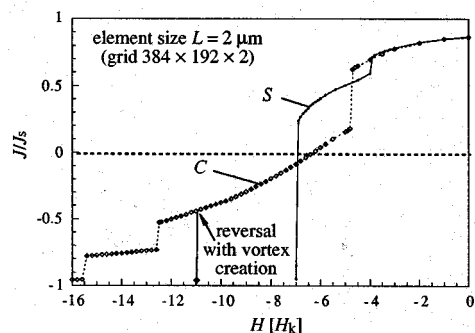
Fig. 18. Demagnetization curves for C and S configurations for the element size $L = 2\ \mu$m. Loops represent the magnetization curves found on the grid with $384 \times 192 \times 2$ cells. Other reversal mode by the vortex creation, observed with $256 \times 128 \times 4$ cells, is also indicated.
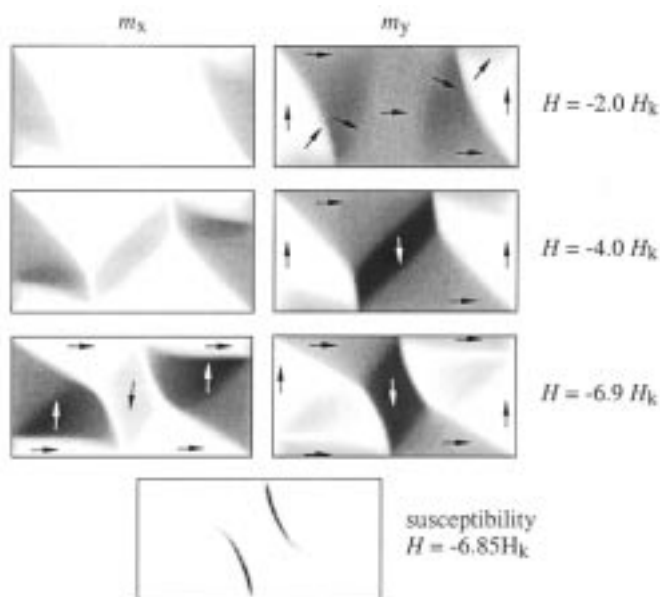

Fig. 19. Development of the S state concertina pattern with a first irreversible process at a field of $-3.9\ H_k$. Again, a configuration with three transverse domains leads to magnetization reversal with the same nucleation mode as for $L = 500$ nm, which is shown by the susceptibility map.

Fig. 20. Development of the C state concertina and the ensuing magnetization reversal. First irreversible process serves to connect the edge domains, eliminating two transverse domains. Second configuration change leads to the formation of a 360° wall, when the lower edge of the element is touched by the domain walls. Final reversal needed a third irreversible process and was achieved when the remaining horizontal walls touched the upper edge.

domains branched off from the edge domains get connected, a relatively stable three-domain configuration is created. The switching field is reduced from 30.7 H_k at $L = 0.5\ \mu$m to approximately 7.0 H_K for this element size. The reversal mode remained the same as for the smaller element; i.e., the susceptibility maximum lay still in the curved inner walls.

For the C state, the behavior became more complicated for $L = 2\ \mu$m than it was found in the smaller element. A first magnetization jump occurred at about $-4.7\ H_k$. At this field, two of the four transverse domains of the concertina collapsed, and the edge domains became interconnected. With a further decreasing field, the remaining two transverse domains grew steadily, accompanied by a gradual rotation of the magnetization in their interior (see Fig. 20).

By this process, a rather high negative magnetization was reached. The configuration appeared remarkably stable and was only destroyed when the lower horizontal walls of the transverse
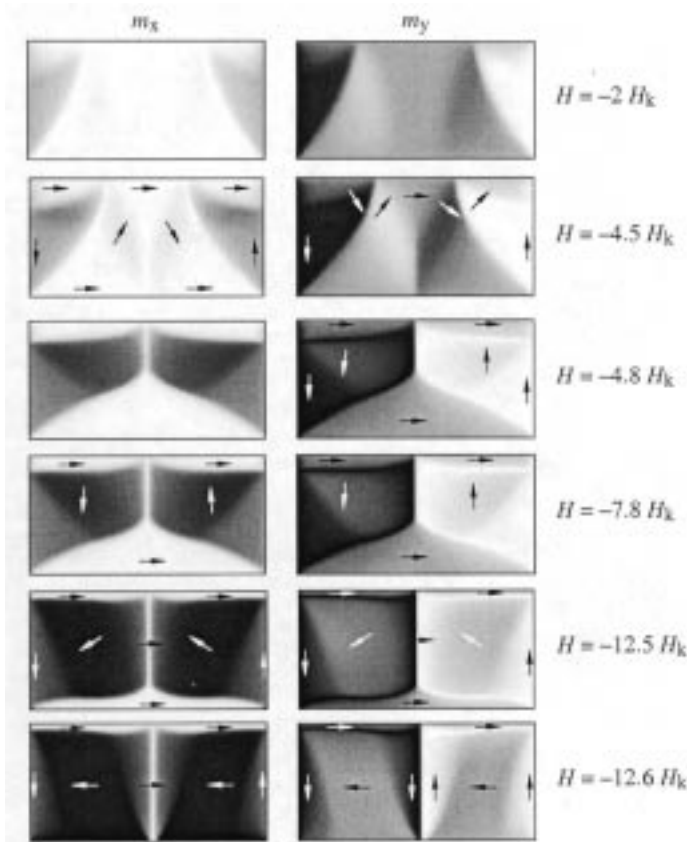
domains touched the lower long edge. The resulting collapse of the transverse domains led to the formation of a 360° wall in the middle of the element. Finally, this wall was also destroyed by a third irreversible process at $-15.5\ H_k$, when the remaining horizontal walls reached the upper edge completing the inversion of the C state.

Although this reversal mode was observed with $384 \times 192 \times 2$ cells, another possible reversal mechanism was noticed ("unfortunately") on a grid with $256 \times 128 \times 2$ cells. In this case, a vortex was generated at the wall cluster in the middle of the upper long edge, which entered the 180° wall at a field of -11 H_k. This is illustrated by a transient state in Fig. 21, where the two shallow domains at the upper edge and the transverse domains are already almost reversed (note the tiny black dot in the m_z-component).

From this, it is difficult to decide which one is the true reversal mode. Although we have the tendency to believe that the result on the finer grid is the correct one, only another calculation on an even finer grid, which we could not perform any more, could have supported this supposition. Thus, the benchmark problem conserves yet another riddle, which waits to be unveiled.

Another observation might be interesting in this context. Namely, the immediate argument that the omission of the precession term in our method suppresses the vortex formation
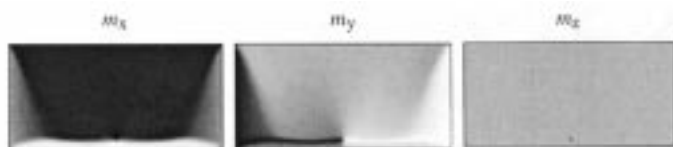
Fig. 21. Alternative reversal mode of the C state for $L = 2 \mu$m by the generation of a vortex. Note that a transient state is shown here. Vortex entered from the upper long edge and is visible in the m_z-magnetization map as a small black dot.

and makes the occurrence of the 360° wall possible is not so straightforward either. When we looked closer at the components of the effective field, we found that its y-component, which could generate the vortex by a torque on the magnetization oriented along x, just passes through zero, where the wall is located and the vortex should be generated. In fact, this is just the reason why the wall is sitting there. In addition, the high symmetry of the situation leads to a degeneracy with respect to the sign of the m_z-component. In this respect, the situation is resembling the type of "catastrophic" switching discussed in [32]. Altogether, the rich variety of solutions that can be found in such seemingly simple situations is remarkable. From the experiment, 360° walls are well known, and in practice, both reversal mechanisms that appear not to be separated by a large energy barrier probably play a role. A dynamical calculation would be very desirable for such a case.

ACKNOWLEDGMENT

REFERENCES

[1] W. F. Brown, Jr., *Micromagnetics*. New York: Wiley, 1963.
[2] Micromagnetic Modeling Activity Group, National Institute of Standards and Technology. [Online]. Available: http://www.ctcms.nist.gov/~rdm/mumag.html
[3] A. Aharoni, "Incoherent magnetization reversals in elongated particles," in *Proc. EMMA'98, Zaragoza, J. Magn. Magn. Mater.*, vol. 196, 1999, pp. 786–790.
[4] ——, "Critique on the numerical micromagnetics of nano-particles," *J. Magn. Magn. Mat.*, vol. 203, pp. 33–36, 1999.
[5] *'Magnetic Microstructure' Workshop*. Leipzig: Max-Planck-Institut for Mathematics in the Sciences by Antonio de Simone, Oct. 1998.
[6] Y. Zheng and J. Zhu, "Switching field variation in patterned submicron magnetic film elements," *J. Appl. Phys.*, vol. 81, pp. 5471–5473, 1997.
[7] D. R. Fredkin and T. R. Koehler, "Numerical micromagnetics by the finite element method," *IEEE Trans. Magn.*, vol. MAG-23, pp. 3385–3387, 1987.
[8] ——, "Finite element methods for micromagnetics," *IEEE Trans. Magn.*, vol. 28, pp. 1239–1244, 1992.
[9] Y. Nakatani, Y. Uesaka, and N. Hayashi, "Direct solution of the Landau–Lifshitz–Gilbert equation for micromagnetics," *Jpn. J. Appl. Phys.*, vol. 28, pp. 2485–2507, 1989.
[10] T. Schrefl and J. Fidler, "A higher-order FEM-BEM method for the calculation of domain processes in magnetic nano-elements," *IEEE Trans. Magn.*, vol. 33, pp. 4182–4184, 1997.
[11] R. Hertel and H. Kronmüller, "Adaptive finite element mesh refinement techniques in three-dimensional micromagnetic modeling," *IEEE Trans. Magn.*, vol. 34, pp. 3922–3930, 1998.
[12] K. J. Kirk, J. N. Chapman, and C. D. W. Wilkinson, "Switching fields and magnetostatic interactions of thin film magnetic nanoelements," *Appl. Phys. Lett.*, vol. 71, pp. 539–541, 1997.
[13] J. McCord, A. Hubert, and A. Chizhik, "Domains and hysteresis in patterned soft magnetic elements," *IEEE Trans. Magn.*, vol. 33, pp. 3981–3983, 1997.
[14] H. A. M. v. d. Berg, "Domain structures in soft-ferromagnetic thin-film objects," *J. Appl. Phys.*, vol. 61, pp. 4194–4199, 1987.
[15] ——, "Self-consistent domain theory in soft-ferromagnetic media II: Basic domain structures in thin-film objects," *J. Appl. Phys.*, vol. 60, pp. 1104–1113, 1986.
[16] W. Rave, K. Ramstöck, and A. Hubert, "Corners and nucleation in micromagnetics," *J. Magn. Magn. Mater.*, vol. 183, pp. 328–332, 1998.
[17] W. Rave, K. Fabian, and A. Hubert, "Magnetic states of small cubic particles with uniaxial anisotropy," *J. Magn. Magn. Mater.*, vol. 190, pp. 332–348, 1998.
[18] FFTW Package, M. Frigo and S. G. Johnson. [Online]. Available: http://theory.lcs.mit.edu/~fftw/
[19] A. Hubert and M. Rührig, "Micromagnetic analysis of thin-film elements," *J. Appl. Phys.*, vol. 69, pp. 6072–6077, 1991.
[20] H. Riedel and A. Seeger, "Micromagnetic treatment of Néel walls," *Phys. Stat. Sol. b*, vol. 46, pp. 377–384, 1971.
[21] A. Hubert and R. Schäfer, *Magnetic Domains—The Analysis of Magnetic Microstructures*. New York: Springer-Verlag, 1998, p. 324.
[22] L. Néel, "Energies des parois de Bloch dans les couches minces," *Comp. Rend. Acad. Sci. Paris*, vol. 241, pp. 533–536, 1953.
[23] A. Holz and A. Hubert, "Wandstrukturen in dünnen magnetischen Schichten," *Z. Angew. Phys.*, vol. 26, pp. 145–152, 1969.
[24] J. Zhu, Y. Zheng, and X. Lin, "Micromagnetics of small size patterned exchange biased Permalloy film elements," *J. Appl. Phys.*, vol. 81, pp. 4336–4341, 1997.
[25] A. Hubert, W. Rave, and S. L. Tomlinson, "Imaging magnetic charges with magnetic force microscopy," *Phys. Stat. Sol. b*, vol. 204, pp. 817–828, 1997.
[26] D. V. Berkov, "Numerical calculation of the energy barrier distribution in disordered many-particle systems: The path integral method," *J. Magn. Magn. Mater.*, vol. 186, pp. 199–213, 1998.
[27] K. Ramstöck, "Numerical calculation of the energy barrier distribution in disordered many-particle systems: The path integral method," Ph.D. dissertation, University Erlangen-Nürnberg, Germany, 1997.
[28] D. Berkov, K. Ramstöck, and A. Hubert, "Solving micromagnetic problems toward an optimal numerical method," *Phys. Stat. Sol. a*, vol. 137, pp. 207–225, 1993.
[29] K. Ramstöck, T. Leibl, and A. Hubert, "Optimizing stray field computations in finite-element micromagnetics," *J. Magn. Magn. Mater.*, vol. 135, pp. 97–110, 1994.
[30] W. F. Brown, Jr. and A. E. LaBonte, "Structure and energy of one-dimensional domain walls in ferromagnetic thin films," *J. Appl. Phys.*, vol. 36, pp. 1380–1386, 1965.
[31] W. H. Press, S. A. Teukolsky, W. T. Vetterling, and B. P. Flannery, *Numerical Recipes in FORTRAN: The Art of Scientific Computing*. Cambridge: Cambridge Univ. Press, 1992.
[32] A. Hubert and W. Rave, "Systematic analysis of micromagnetic switching processes," *Phys. Stat. Sol. b*, vol. 211, no. 2, pp. 815–829, 1999.

Wolfgang Rave (S'86–M'89) was born in Stuttgart, Germany, in 1960. He received the Diploma Thesis degree graduated in material science of electrical engineering from the University of Erlangen-Nürnberg in 1985.

After a year at the Magnetics Technology Center, Carnegie Mellon University, Pittsburgh, PA, he returned to Erlangen to pursue the quantitative Kerr-method with Alex Hubert in his Ph.D. dissertation until 1990. Thereafter, he worked for two years at the German company AEG as a Development Engineer for infrared detector readout circuits. From 1993 to 1994, he spent two years at the University of Paris-Sud, Orsay, France, working on magnetic force microscopy. This stay introduced him to numerical micromagnetics, a subject he pursued intensely since 1995 in Dresden, where he worked in close collaboration with Alex Hubert and Rudolf Schäfer. Since May 1999, he has been working on mobile communications at Dresden University.

Alex Hubert (M'96–SM'96) was born in Darmstadt, Germany, in 1938. He received the Diploma Thesis and the Ph.D. degrees in physics from Bonn and Munich.

From 1966 to 1973, he was with the Max Planck Institut für Metallforschung in Stuttgart, where he specialized on the micromagnetic study of magnetic domain walls. This led to the "discovery" of the two-dimensional vortex structure of asymmetical Néel and Bloch walls and to his inaugural dissertation "Theorie der Domänenwände in geordneten Medien," which was also published as a book. In 1975, he became a Professor for Material Science at The University of Erlangen. There, he set up a lab, which became well known for magnetic imaging using the Kerr effect and numerical micromagnetic investigations. In 1998, together with his coauthor Rudolf Schäfer, he published a book containing his life long experience with magnetic microstructures: *Magnetic Domains—The Analysis of Magnetic Microstructures*. He spent sabbaticals at the IBM Research Center in Yorktown Heights, the Magnetics Technology Center of Carnegie Mellon University, Pittsburgh, the Institut für Physikalische Hochtechnologie Jena, and the Institut für Festkörper- und Werkstofforschung, Dresden.

Dr. Hubert died, much too early, on February 16, 1999.